# Antiphase Boundaries in Truncated Octahedron-shaped Zn-doped Magnetite Nanocrystals

Nerio Fontaiña-Troitiño,[a] Miguel A. Ramos-Docampo,[a] Martín Testa-Anta,[a] Benito Rodríguez-González,[a] Manuel Bañobre-López, [b] Laura Bocher,[c] Keith P. McKenna[d] and Verónica Salgueiriño,*[a]

**The presence of antiphase boundaries with a local ferromagnetic coupling is herein related to the magnetic performance of truncated octahedron-shaped zinc-doped magnetite nanocrystals. Atomic resolution STEM imaging reveals the presence of these antiphase boundaries perpendicular to the [111] direction of the spinel structure of the nanocrystals. Magnetic characterization and DFT calculations indicate a local ferromagnetic order, originated from a Fe-Fe enrichment at these individual lattice defects in the nanocrystals, as the underlying cause of the magnetic response registered.**

## Introduction

The macroscopic magnetic and electric properties of transition metal oxides can be engineered by modifying ferroic atomic displacements in the crystalline lattice, which cause different effects due to the modified ionic bonding,[1] for example, at antiphase boundaries (APBs). The APBs are non-equilibrium features of crystalline solids. Since they imply a positive excess of free energy, in polycrystalline materials these interfacial grain boundaries evolve to reduce their area while attaining particular local atomic arrangements.[2] In magnetic materials, understanding spin order in these interface regions is key for materials science-based technologies, keen to take advantage of the relationship between magnetism and structural disorder within the APBs.[3] In fact, the atomic disorder at the interface region can deteriorate the ferromagnetic spin order in alloys,[4] but can as well serve as sources of ferromagnetism,[5,6] rendering the APBs promising functionalities related to the pinning of magnetic domain walls or to inducing large critical fields for magnetic saturation.[7] Epitaxial thin films containing APBs have been therefore widely studied, given the potential advantages they can offer in the development of spintronic devices.[8,9]

However, very few reports mention directly APBs in nanoparticles,[10] likely because their final arrangement within the crystalline lattice may be governed by the shape and topological nature of the nanocrystal itself, removing them if relaxed, for example when attaining the spherical shape.[11] On the other hand, nanoparticles are usually characterized by lattice defects, mainly at the surface, which often degrade their functionality. Therefore, magnetic nanoparticles are usually characterized by a reduced magnetization, relative to that of the bulk and attributed to surface spin disorder and surface spin canting.[12] Alternatively, the presence of dislocations and twin boundaries has been associated to large discrepancies between the magnetic and geometric size distribution,[13] and highly strained regions inside nanoparticles were also related to magnetic disorder.[14] Yet, the APBs, as lattice defects that can work as sources of strong antiferromagnetic interactions, can as well explain the reduced values of magnetization in nanoparticles.[10]

On the other hand, polyhedron shaped nanoparticles can establish a particular magnetic arrangement within the nanocrystal, given the higher compressive strain compared to that in the bulk material. In this situation, the surface atoms in the facets do not remain at the bulk parameter but contract, producing strain to reduce surface stress and endorsing the crystalline lattice with defects. The magnetic surface anisotropy resulting from the characteristically lower symmetry at the surface can favor in and out of plane orientation of the magnetic moments at the surface facets,[15] and the interplay between surface and bulk magnetic anisotropies and exchange interactions results in non-collinearities of the whole spin structure.[16] Consequently, the appropriate nanoscale engineering of APBs can drive the magnetic performance of nanocrystals. This is particularly interesting in spinel ferrites,[17,18] which show a large variety of electronic and magnetic properties, and where APBs can become a driving force for the development of future electronic and magnetic device applications,[19] for example through the generation of spin-polarized currents in ferrite-based tunnel junctions. In particular, a suitable material fulfilling these characteristics is the magnetic spinel oxide $Zn_xFe_{3-x}O_4$, in which the magnetic and electric properties can be tuned by the concentration of Zn.[20,21]

Accordingly, herein, we study truncated-octahedron shaped nanocrystals of magnetite, which have been doped with Zn while keeping the spinel structure and which appear endorsed with APBs. While the strain stemming from the polyhedron shape of the nanocrystals likely avoids the evolution of these APBs to attain defect-free single crystals, their disposition perpendicular to the [111] direction of the crystalline structure implies an additional local ferromagnetic coupling. Density functional theory calculations point to a disruption in the structural order stemming from the APBs as a source of Fe-Fe pairs, which modify the magnetic performance of the nanocrystals, and render the APBs new functionalities at the nanoscale.

## Results and Discussion

The stoichiometry of zinc-doped magnetite nanoparticles herein studied was adjusted with the relative proportion of zinc and iron precursors to obtain $Zn_xFe_{3-x}O_4$, with $x$ = 0.25 (sample ***1***), $x$ = 0.50 (sample ***2***), $x$ = 0.80 (sample ***3***) and $x$ = 1.00 (sample ***4***). The synthesis (see experimental section in the electronic supplementary information (ESI)) promotes the formation of truncated octahedron-shaped nanoparticles, even without the presence of specific ligands or capping agents but just trioctylamine molecules, which work as solvent and control the nucleation and the growth of the nanocrystals in solution.

Figure 1. HRTEM images of representative zinc-doped magnetite nanocrystals (a, d). Atomically resolved HAADF-STEM images at the edge of single $Zn_{0.25}Fe_{2.75}O_4$ (b) and single $Zn_{0.50}Fe_{2.50}O_4$ (e) truncated octahedron-shaped nanocrystal along the [1-10] zone axis and enlarged views of the inverse spinel structure with its atomic structural model along the cubic [1-10] axis (c, f).

As focusing the analysis on the more ferrimagnetic samples, that is, those with the lower doping, figures 1a and 1d include HRTEM images showing representative truncated octahedron-shaped nanoparticles from samples ***1*** and ***2*** under consideration, with eight {111} and six {001} facets. Figure S1 (in the ESI) includes low magnification TEM (left column) and HRTEM (center column) images and shows the particle size distribution (right column), taking into account the larger edge length of the nanocrystals, which are fitted to log-normal functions (with mean */ standard deviation of the four samples synthesized: 15.5 */ 1.4 nm (sample ***1***), 15.0 */ 1.4 nm (sample ***2***), 14.0 */ 1.3 nm (sample ***3***) and 13.5 */ 1.3 nm (sample ***4***)). EDX spectroscopy and ICP analysis confirmed the stoichiometry, quantified in Zn and Fe atomic percentages corresponding to $Zn_{0.25}Fe_{2.75}O_4$ (sample ***1***), $Zn_{0.50}Fe_{2.50}O_4$ (sample ***2***), $Zn_{0.80}Fe_{2.20}O_4$ (sample ***3***) and $Zn_{1.00}Fe_{3.00}O_4$ (sample ***4***).

The nanocrystals from samples ***1*** and ***2*** were studied in detail, first down to the atomic scale highlighting the inverse spinel structure by high-angle annular dark-field (HAADF) STEM, as shown in figures 1 (b, c (sample ***1***), and e, f (sample ***2***)). From the HAADF intensities of the HAADF-STEM images obtained along the [1-10] zone axis, two types of contrast are distinct, revealing solely the Fe atomic columns' positions. We have to take into account that the HAADF intensity of the oxygen atoms remains negligible with respect to that of Fe in the HAADF imaging conditions. Figures 1c and 1f present enlarged views of the defect-free spinel structure, where a structural model with Fe atomic columns emphasizing the local arrangement of

tetrahedral $Fe^{3+}$ sites (light blue) and octahedral $Fe^{2+}$ sites (dark blue) along the [1-10] zone axis, is included. The interatomic distances extracted from the atomic columns' projection along the [1-10] zone axis confirm a slight increase of the bulk cell parameter compared to the magnetite (0.8384 nm) as expected when doping the $Fe_3O_4$ lattice with $Zn^{2+}$ cations. Additionally, there may be some reconstruction at the surface, likely stemming from an initial instability at different spinel surface planes. Similar results were reported for lithium manganese oxide with a spinel structure ($LiMn_2O_4$),[22] on which this surface reconstruction was described to create a more stable cation-dense surface layer that is also oxygen-deficient.[23]

The high degree of crystallinity of the nanoparticles from samples ***1*** and ***2*** shown in the HRTEM images is also reflected by the X-ray diffraction (XRD) patterns included in figure 2 (a and b), which also gives us a more global overview of the crystallography of the samples. The diffracted peaks are fully attributable to the $Zn_xFe_{3-x}O_4$ spinel structure (*Fd-3m* space group) and no extra-peaks from impurities were observed. The indexation was carried out using reference values from the Crystallography Open DataBase (in blue). In order to obtain more information about the two samples, a Rietveld refinement was performed using the software Rietica. The cell parameter *a* was calculated to be 0.8427 and 0.8429 nm for samples ***1*** and ***2*** respectively, which is slightly higher than the value of magnetite (0.8384 nm). Taking into account the larger ionic radius of $Zn^{2+}$ in comparison to that of the $Fe^{2+}$ cations, the lattice constant is anticipated to increase along with the Zn content in the final nanostructure, confirming therefore the uniform Zn doping.

Raman spectroscopy is also a very useful technique to study and explore the crystalline lattice of nanomaterials.[24-27] According to the group theory, the zinc ferrite presents the following phonon modes:

$$\Gamma = A_{1g}(R) + E_g(R) + T_{1g} + 3T_{2g}(R) + 2A_{2u} + 2E_u + 4T_{1u}(IR) + 2T_{2u}$$

out of which five are Raman active (indicated with *(R)*). Three main bands centered at 333-338, 452-462 and 676 $cm^{-1}$ can be observed in the Raman spectra included in figure 2 (using excitation wavelengths $\lambda$ = 532 nm (c, d) and $\lambda$ = 633 nm (e, f)), which correspond to the vibrational modes $T_{2g}$ *(2)*, $T_{2g}$ *(3)* and $A_{1g}$, respectively. The observed Raman modes were fitted to Lorentzian curves, permitting therefore a closer inspection. While the 532 nm-excitation wavelength spectra (in figure 2 (c and d)) indicate some residual oxidation, as reflected by the additional small band at 708 $cm^{-1}$, typically associated to maghemite,[28] the 633 nm-excitation wavelength spectra (in figure 2 (e and f)) can resolve the $A_{1g}$ band, which is found to split into two different modes,[29-31] centered at 651 and 680 $cm^{-1}$ for sample ***1***, and 648 and 680 $cm^{-1}$ for sample ***2***. Though slightly blue-shifted if compared to bulk, the Raman shift at 680 $cm^{-1}$ matches the Fe-O stretching vibration at the tetrahedral void characteristic of pure magnetite. Indeed, magnetite is a mixed-valence compound and is expected to show a very intense and symmetric $A_{1g}$ band, without visible features of different intensities due to the different positions of iron sites in the inverse spinel structure, owing to its delocalized electronic structure.[32] Consequently, the appearance of a shoulder about 648-651 $cm^{-1}$ (in violet) indicates the presence of $Zn^{2+}$ cations being incorporated into the tetrahedral voids, attending to the generic formula of a normal spinel $(Zn^{2+})_A(Fe^{3+})_BO_4$, and considering the theoretical tetrahedral site preference ($Zn^{2+}$ > $Fe^{3+}$ > $Fe^{2+}$).[33,34]

Figure 2. XRD patterns and Rietveld analysis (a, b) and Raman spectra registered using two excitation wavelengths ($\lambda$ = 532 nm (c, d) and $\lambda$ = 633 nm (e, f)) from sample ***1*** (framed in black) and sample ***2*** (framed in red).

The magnetic behavior of these zinc-doped magnetite nanocrystals was checked, measuring the field and temperature dependent magnetic response of the four samples (***1***, ***2***, ***3***, and ***4***) (see figures S2 and S3 in the ESI). The field-dependent magnetization curves (*M-H*) of samples ***1*** and ***2*** are compared in figures 3a and b (at 300 K and at 5 K, respectively). The saturation magnetization ($M_S$) of these nanoparticles depends on the stoichiometry given by *x*, with larger values of $M_S$ for sample ***2***. Indeed, it is well known that when adding $Zn^{2+}$ cations (non-magnetic, $[Ar]3d^{10}$ configuration) to spinel ferrites, their magnetization increases with Zn content, up to values of *x* = 0.5 ($Zn_xFe_{3-x}O_4$), and drops for higher values of *x*,[35,36] as shown in figure S2 (in the ESI), on which this tendency can be appreciated. Figures 3c and d compare the ZFC - FC temperature-dependent magnetization curves of samples ***1*** and ***2***. The blocking temperature ($T_B$), defined as the maximum of the ZFC curve and representing the temperature at which the thermal energy becomes comparable to the anisotropy energy barrier, was found to be $T_B$ ~ 230 K (sample ***1***) and $T_B$ ~ 245 K (sample ***2***). Besides the effective magnetic anisotropy of the nanocrystals, the values registered for $T_B$ also stem from the magnetic dipolar interactions between them and the particle size distribution. Given the similar particle size distribution in both samples, the large magnetic moment of the Zn-doped nanoparticles (as

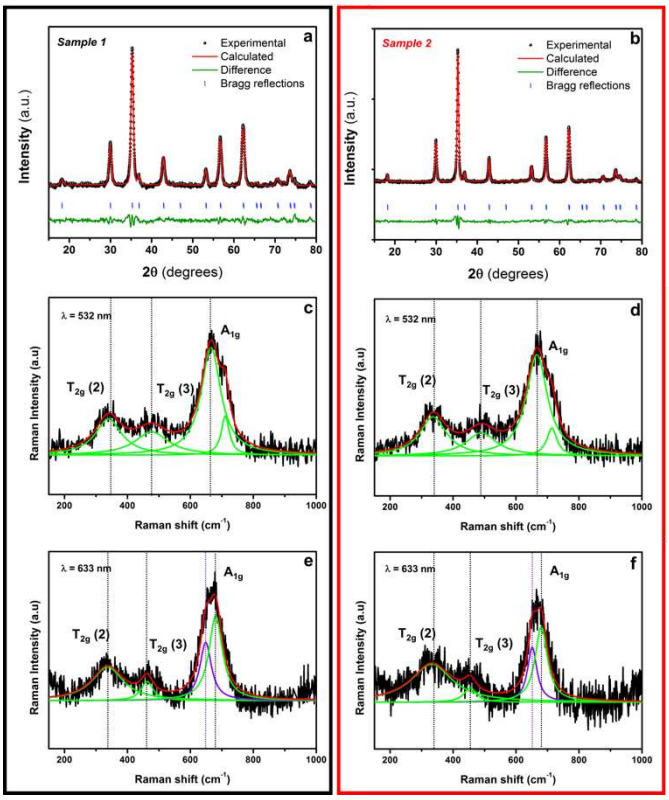

estimated from the values of saturation magnetization ($\mu$ = 5.54 x $10^5$ (sample ***1***) and $\mu$ = 6.11 x $10^5$ $\mu_B$/particle (sample ***2***) (at 5K)), can be the underlying factor responsible for the increase of the magnetic dipolar interactions, and therefore for the increase in the energy barrier, which justify the shift of $T_B$ to the values registered, despite the relatively small size of the nanoparticles. Figure S3 includes the comparison of the ZFC-FC magnetization curves of the four samples with different Zn content, highlighting the transition from the ferrimagnetism of the samples with the lower Zn doping (samples ***1*** and ***2***) to the antiferromagnetism of the samples with the higher Zn doping (samples ***3*** and ***4***). The consequent decrease in the total magnetic moment of the nanoparticles for $x > 0.5$ also implies a decrease in the blocking temperature.

Another observation in the ZFC - FC magnetization curves of samples ***1*** and ***2*** is the absence of a Verwey transition, characteristic of magnetite. The Verwey transition and the magnetism of the $Fe_3O_4$ phase are both related to the metal-to-oxygen stoichiometry.[37,38] A reduction of the lattice parameter and the Verwey transition temperature can be detected as the cation vacancies increase and consequently, in a non-stoichiometric $Fe_{3-\delta}O_4$ sample with $\delta$=0.066,[39] the Verwey transition almost disappears. Analogously, the Zn content instead of Fe vacancies has a similar effect in both samples ***1*** and ***2***, justifying the absence of the Verwey transition and consequently revealing the homogeneous doping.

Figure 3. Field-dependent magnetization curves (*M-H*) at 300 K (a) and at 5 K (b), ZFC-FC temperature dependent magnetization curves (c, d) under an applied magnetic field of 5 mT for samples ***1*** and ***2***, respectively. Field-dependent magnetization (at 5 K) (e) and temperature-dependent saturation magnetization ($\mu_0$H = 2 T) (f), both fitted to the Bloch law for samples ***1*** and ***2***.

These truncated-octahedron shaped nanocrystals show similar values of saturation magnetization if compared with polyhedral,[40] but larger values if compared to spherical Zn-doped magnetite nanoparticles.[41,42] The polyhedron morphology implies a situation of enclosed strain that is released in the case of the spherical nanoparticles with a disordered surface. This strain at the surface facets can promote the formation of internal lattice defects, such as ferromagnetically coupled APBs, which can be related to this magnetic enhancement.[43] APBs in nanoparticles are defects associated to stacking faults in the cation sublattice. The distinct type of APBs in which the ferromagnetic spin order is not appreciably depressed but can be even increased, was investigated by Murakami *et al*. in thin films, who reported an enhanced magnetization due to structural disorder within a nanometer-scale interface region.[3] Moussy *et al*. also explored APBs, perpendicular to the [111] direction of the crystalline structure of $Fe_3O_4$ thin films but antiferromagnetically coupled.[44] Therefore, a differentiated magnetic behavior can be explained taking into account the presence of these APBs, considering a model that describes the approach to saturation of two semi-infinite media separated by Bloch walls, neglecting the anisotropy energy and considering only the competition between Zeeman energy, which favors magnetization alignment along the applied magnetic field and the exchange energy.[8] In this situation, the minimization of the energy yields the magnetic field dependence of the magnetization of equation 1:

$$M = M_S\left(1 - \frac{b}{H^n}\right)$$

where $M$ is the magnetization, $M_S$ the saturation magnetization, $b$ a parameter related to APB density and $n$ = 0.5 in this model.[44] The magnetic response of samples ***1*** and ***2*** at 5 K can be fitted to equation 1 when applying a magnetic field up to 4.5 T (figure 3e), with values of $M_S$ = 108 Am$^2$/kg and $b$ = 0.070 (T$^{1/2}$) for sample ***1*** and $M_S$ = 119 Am$^2$/kg and $b$ = 0.066 (T$^{1/2}$), for sample ***2***. The value of $b$ quantifies the approach to saturation of the system, and indicates that it is slightly faster for sample ***1***.

Additionally, the magnetic dynamics in nanoparticles below the blocking temperature is expected to be dominated by uniform excitations of spin waves, leading to a (size-dependent[45]) linear temperature dependence of the magnetization, in contrast to the Bloch $T^{3/2}$ law in bulk materials, below the Curie or Néel temperature.[46] However, the temperature dependence of the saturation magnetization (applying a magnetic field $\mu_0 H$ = 2 T) for the two samples (shown in figure 3f), have the data fitted (solid lines in the graph) to the Bloch law:

$$M_S(T) = M_{S_0}[1 - BT^{\alpha}]$$

with *B* and $\alpha$ being the Bloch constant and Bloch exponent ($\alpha$ =1.5),[47] respectively. The very good agreement below 230 K and below 245 K (that is, below the average blocking $T_B$ of both samples) suggests a bulk-like behavior in both nanoparticulated samples, likely because of the very good crystallinity and the dipolar interactions between nanoparticles, which then respond collectively to the magnetic field, with very uniform excitations within the samples. Accordingly, considering the model above described about the approach to saturation of semi-infinite media separated by Bloch walls, the magnetic field and temperature dependence of the magnetization can be related to the presence of APBs; from structural defects in the crystalline lattice of the nanoparticles or to interfaces between the touching facets of two nanoparticles. In the first case, the approach to saturation of both samples would be described in terms of magnetic domains with coupled APBs, which, if ferromagnetically coupled, would lead to an estimated saturation magnetization larger than the values expected for bulk or for spherical nanoparticles with similar sizes and composition. In this regard, Eerestein *et al.* have proposed different magnetic exchange interactions competing across these boundaries,[48,49] but in this case, the slightly increased values of saturation magnetization would be indicative of ferromagnetic (parallel) exchange interactions stabilized by an APB. Consequently, understanding the relationship between magnetism and structural disorder within the APBs,[3] and predicting their atomic-scale structure and properties would help to understand their impact on the magnetic response, which can be critical because of the anomaly they imply.

Accordingly, in order to shed light over this issue, the APBs present in the nanoparticles were consequently studied by STEM imaging. Figures 4a and b include HAADF-STEM images showing an APB perpendicular to the [111] direction in one of the truncated octahedron-shaped $Zn_{0.25}Fe_{2.75}O_4$ nanocrystals (check the yellow arrows included to guide the eye). The atomically resolved HAADF-STEM image in figure 4b reflects the broken translational symmetry, so that structural domains are visible. This observed structural defect is an antiphase domain boundary which can be described by a fractional unit cell shift in the [1 0 -1] direction. It can be also described as a stacking defect in the cation sublattice, by which the oxygen lattice should remain undisturbed across the APB while the cation lattice is shifted by a <1 0 -1> translation vector. Since the only visible APBs are the ones whose translation vector is perpendicular to the reflection used to obtain the dark-field TEM images, the real APB density can be actually higher than the observed by TEM,[44] in both samples ***1*** and ***2***.

These APBs working as sources of structural disorder can be produced by dislocation movement or be thermally induced. Depending on the synthetic method, they can be produced by heat treatment, via nucleation, growth and impingement of individual ordered regions. Alternatively, we can consider the multiple coalescence events associated with very small nanocrystals while growing, attributed to their larger surface fraction and energies, and increased mobility and collision frequency.[50,51] If the initial coalescence of very small crystalline nuclei proceeds along a specific crystallographic orientation, corresponding for example to the fusion of shifted {111} facets, APBs can become stable while the nanocrystals gradually evolve into the truncated-octahedra finally attained. In general, the synthetic methods promoting the synthesis of polyhedron-shaped nanocrystals imply the production of strained crystalline structures which are not able to get rid of defects, and accordingly, the nanocrystals will appear endorsed with defects such as these antiphase boundaries. The key issue then is about having control on fixing the antiphase boundaries in particular crystallographic directions.

As indicated in the STEM images in figure 4 the APB separates ordered regions showing a definite change in the atomic sequence. Figure 4b even shows the finite thickness within which the degree of atomic order is depressed. Indeed, the gradual steps of the APB across the nanocrystal are visible, offering as well a finite width of atomic disorder of 3-4 atoms. Allen and Cahn have theoretically indicated that gradual changes in the order parameter can reduce the free energy in the interface region,[2] and so, this disorder can cause an enrichment of Fe content, affecting the number of nearest Fe-Fe pairs,[3] with a critical impact on the local spin order of the APB and the global spin order of the material. Accordingly, and to further consolidate the hypothesis by which the magnetic response of the nanocrystals would benefit from the APBs, we have performed density functional theory (DFT) calculations, to predict the structure, electronic and magnetic properties of both bulk $Zn_xFe_{3-x}O_4$ and an associated APB perpendicular to the [111] direction, using the projector augmented wave method as implemented in the Vienna *ab initio* simulation package.[52,53] This approach has been used in a previous report to model the (110) APB in $Fe_3O_4$ where the predicted structure was confirmed to be in excellent agreement with atomic scale STEM imaging.[19] The predicted properties of bulk $Zn_xFe_{3-x}O_4$ (*x* = 0.00, *x* = 0.25, *x* = 0.50, *x* = 0.75 and *x*= 1.00) at the different levels of theory are discussed in detail in the ESI. Summarizing this analysis, we find that both PBE and PBE+*U* give reasonable predictions for the stable magnetic configuration of $Zn_xFe_{3-x}O_4$ phases with the latter slightly more consistent with the predictions of HSE, which is expected to be more accurate (especially for the insulating phases). As the concentration of Zn increases we predict a slight lattice expansion along with the expected increase in the magnetic moment, as reflected in the magnetic measurements. A clear crossover between ferrimagnetic and antiferromagnetic order between *x* = 0.75 and *x* = 1.00 is also predicted (see Table S1 in the SI). Focusing the analysis on

sample ***1*** we build the supercell for the (111) APB as described in the experimental section, based on the appropriate bulk lattice constant (i.e. a = 8.442 Å for PBE and a = 8.512 Å for PBE+*U* – see Table I in the SI). The supercell has six Zn ions distributed homogeneously over the tet-Fe sites (i.e. $Zn_{12}Fe_{132}O_{192}$) consistent with the prediction for the bulk crystal with no Zn clustering. The optimized structure of the APB supercell is shown in figure 4c which is structurally similar when viewed along any of the {2,-1,-1} directions (only the presence of Zn ions breaks this symmetry). There is a notable disruption in the structural order next to the APB defect – particularly in the oct-Fe layer near the interface (indicated with a vertical dotted black line to guide the eye).

Figure 4. HAADF-STEM images of a $Zn_{0.25}Fe_{2.75}O_4$ nanocrystal showing an APB (a, b). Optimized structure of an APB perpendicular to the [111] direction (vertical dotted black line to guide the eye) in the $Zn_{0.25}Fe_{2.75}O_4$ crystalline structure on which silver, brown and red spheres represent Zn, Fe and O atoms respectively (c). The same optimized structure with spin density iso-surfaces to indicate the magnetic order (d). Blue and green iso-surfaces represent spin up and spin down, respectively. Note that all oct-Fe sites are spin up while all tet-Fe sites are spin down, according to a ferrimagnetic ground state.

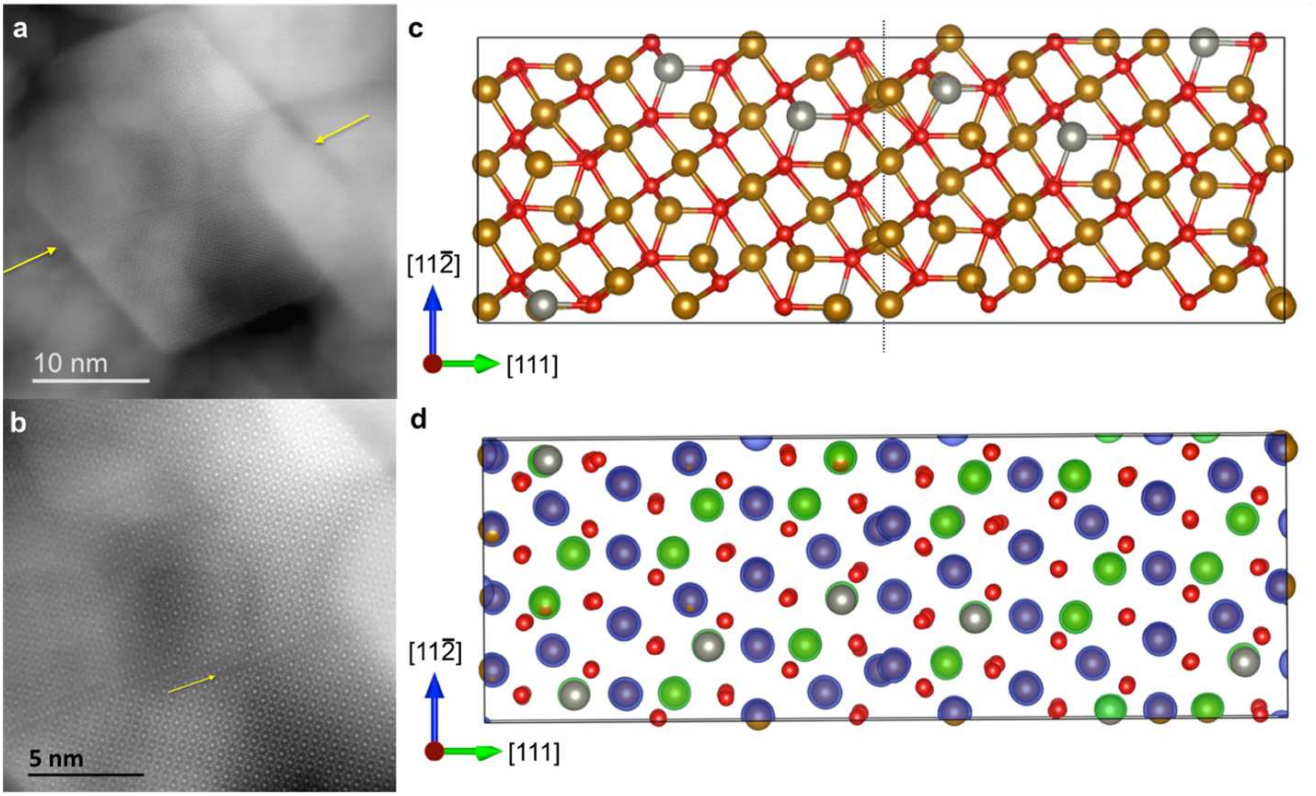


To assess the impact of the APB on the local magnetic order we consider a number of different magnetic configurations and compute their relative stability. The most stable structure is predicted to be ferrimagnetic with no antiferromagnetic coupling across the APB defect, as reflected schematically in figure 4d. The calculated formation energies of the APB (with respect to the bulk) are 0.72 $Jm^{-2}$ using PBE and 0.77 $Jm^{-2}$ using PBE+*U* with no significant difference in optimized atomic structure. This can be rationalized since there are no $Fe_{tet}$-O-$Fe_{tet}$ or $Fe_{oct}$-O-$Fe_{oct}$ bonds introduced with angles close to 180 degrees that could induce antiferromagnetic coupling through the superexchange mechanism. Whichever, antiferromagnetic coupling between the oct-Fe and tet-Fe sublattices is maintained throughout the supercell resulting in the characteristic ferrimagnetic ground state of these spinel structures.

In summary, the DFT calculations predict the atomic structure of the {111} APB defects observed by STEM in the Zn-doped magnetite nanocrystals and associate them with a low formation energy. This stable predicted configuration also indicates a local ferromagnetic coupling across the APB defect, stemming from a disruption in the structural order, particularly in the oct-Fe layer near the interface, which agrees with the experimentally registered magnetic response.

## Conclusions

In conclusion, we relate the unusually sizable values of saturation magnetization of polyhedron shaped Zn-doped magnetite nanocrystals with {111} APB defects in the spinel structure. The predicted atomic structure and magnetic configuration of the APB in the nanocrystals is supported by the high-resolution electron microscopy analysis and the magnetic characterization. Accordingly, the proposed stable APB induces a local ferromagnetic coupling which offers an alternative in the manipulation of the magnetic behavior for spintronic device engineering, for example, through the generation of spin-polarized currents in ferrite-based tunnel junctions.

## Conflicts of interest

There are no conflicts to declare.

## Notes and references

The authors acknowledge the financial support from the Xunta de Galicia (Regional Government, Spain) under project ED431C 2016-034 and the Spanish Ministerio de Economía y Competitividad under projects CTM2014-58481-R and CTM2017-84050-R. M. A. R.-D. and M. T.-A. acknowledge financial support from the Xunta de Galicia (Regional Government, Spain) under grants 2017 ED481A. K.P.M. acknowledges support from EPSRC (EP/K003151/1, EP/P006051/1 and EP/P023843/1). This work made use of the facilities of Archer, the UK's national high-performance computing service, via our membership in the UK HPC Materials Chemistry Consortium, which is funded by EPSRC (EP/L000202/1).

1 J. B. Goodenough. *Chem. Mater.* 2014, **26**, 820.
2 S. M. Allen, J. W. Cahn. *Acta Metallurgica* 1979, **27**, 1085.
3 Y. Murakami, K. Niitsu, T. Tanigaki, R. Kaimuna, H. S. Park, D. Shindo. *Nature Comm*. 2014, **5**, 4133.
4 S. P. Venkateswaran, N. T. Nuhfer, M. de Graef. *Acta materialia* 2007, **55**, 2621.
5 N. Fontaíña-Troitiño, S. Liébana-Viñas, B. Rodríguez-González, Z. A. Li, M. Spasova, M. Farle, V. Salgueiriño. *Nano Letters* 2014, **14**, 640.
6 Z. A. Li, N. Fontaíña-Troitiño, A. Kovacs, S. Liébana-Viñas, M. Spasova, R. E. Dunin-Borkowski, M. Müller, D. Doenning, R. Pentcheva, M. Farle, V. Salgueiriño. *Scientific Reports* 2015, **5**, 7997.
7 K. D. Belashchenko, V. Antropov. *Phys Rev. B* 2002, **66**, 144402.
8 D. T. Margulies, F. T. Parker, M. L. Rudee, F. E. Spada, J. N. Chapman, P. R. Aichison, A. E. Berkowitz. *Phys. Rev. Lett.* 1997, **79**, 5162.
9 R. G. S. Sofin, H.-C. Wu, I. V. Shvets. *Phys. Rev. B* 2011, **84**, 212403.
10 Z. Nedelkoski, D. Kepaptsoglou, L. Lari, T. Wen, R. A. Booth, S. D. Oberdick, P. L. Galindo, Q. M. Ramasse, R. F. L. Evans, S. Majetich, V. Lazarov. *Sci Reports* 2017, **7**, 45997.
11 M. Mamatkulov, J. S. Filhol. *J. Phys. Chem. C* 2013, **117**, 2334.
12 S. Disch, E. Wetterskog, R. P. Hermann, A. Wiedenmann, U. Vainio, G. Salazar-Álvarez, L. Bergström, Th. Brückel. *N. J. Phys.* 2012, **14**, 013025.
13 B. Luigjes, S. m. C. Woudenberg, R. de Groot, J. D. Meeldijk, H. M. Torres Galvis, K. P. de Jong, A. P. Philipse, B. H. Erné. *J. Phys. Chem. C* 2011, **115**, 14598.
14 M. Levy, A. Quarta, A. Espinosa, A. Figuerola, C. Wilhelm, M. García-Hernández, A. Genovese, A. Falqui, D. Alloyeau, R. Buonsanti, P. D. Cozzoli, M. A. García, F. Gazeau, T. Pellegrino. *Chem. Mater.* 2011, **23**, 4170.
15 D. A. Garanin, H. Kachkachi. *Phys. Rev. Lett.* 2003, **90**, 065504.
16 R. Yanes, O. Chubykalo-Fesenko, H. Kachkachi, D. A. Garanin, R. Evans, R. W. Chantrell. *Phys. Rev. B* 2007, **76**, 064416.
17 J.-M. Li, A. C. H. Huan, L. Wang, Y.-W. Du, D. Feng. *Phys. Rev. B* 2000, **61**, 6876.
18 J.-M. Li, X.-L. Zeng, Z.-A. Xu. *Appl. Phys. Lett.* 2013, **103**, 232410.
19 K. P. McKenna, F. Hofer, D. Gilks, V. K. Lazarov, C. Chen, Z. Wang, Y. Ikuhara. *Nature Comm*. 2014, **5**, 5740.
20 D. Venkateshvaran, M. Althammer, A. Nielsen, S. Geprägs, M. S. Ramachandra Rao, S. T. B. Goennenwein, M. Opel, R. Gross. *Phys. Rev. B* 2009, **79**, 134405.
21 M. Srivastava, S. K. Alla, S. S. Meena, N. Gupta, R. K. Mandal, N. K. Prasad. *New J. Chem.* 2018, **42**, 7144.
22 C. D. Amos, M. A. Roldan, M. Varela, J. B. Goodenough, P. J. Ferreira. *Nano Lett.* 2016, **16**, 2899.
23 R. Benedek, M. M. Thackeray, *Phys. Rev. B.* 2011, **83**, 195439.
24 J. Kreisel, M. C. Weber, N. Dix, F. Sánchez, P. A. Thomas, J. Fontcuberta. *Adv. Func. Mater.* 2012, **22**, 5044.
25 O. Chaix-Puchery, C. Cochard, P. Jadhav, J. Kreisel, N. Dix, F. Sánchez, J. Fontcuberta. *Appl. Phys. Lett.* 2011, **99**, 072901.
26 B. Rivas-Murias, V. Salgueiriño. *J. Raman Spectroscopy* 2017, **48**, 837.
27 R. Otero-Lorenzo, M. A. Ramos-Docampo, B. Rodríguez-González, M. Comesaña-Hermo, V. Salgueiriño, *Chem. Mater.* 2017, **29**, 8729.
28 A. M. Jubb, H. C. Allen. *ACS Appl. Mater. Interfaces* 2010, **2**, 2804.
29 J. Preudhomme, P. Tarte. *Spectrochimica Acta* 1971, **27A**, 845.
30 I. F. Chang, S. S. Mitra, *Advances in Physics* 1971, **20**, 349.
31 C. Pereira, A. M. Pereira, C. Fernandes, M. Rocha, R. Menes, M. P. Fernández-García, A. Guedes, P. B. Tavares, J.-M. Grenèche, J. P. Araújo, C. Freire, *Chem. Mater.* 2012, **24**, 1496.
32 T. Fujii, F. M. F. de Groot, G. A. Swatzky, F. C. Voogt, T. Hibma, K. Okada, *Phys. Rev. B* 1999, **59**, 3195.
33 A. Navrotsky, O. J. Kepla, *J. Inorg. Nucl. Chem.* 1968, **30**, 479.
34 R. C. O'Handley. *Modern Magnetic Materials.* Wiley 2000 (New Jersey, USA).
35 E. V. Gorter, *Nature* 1950, **165**, 798.
36 P. G. Bercoff, H. R. Bertorello. *J. Magn. Magn. Mater.* 2000, **213**, 56.
37 N. Guigue-Millot, N. Keller, P. Perriat, *Phys. Rev. B* 2001, **64**, 012402.
38 M. Testa-Anta, S. Liébana-Viñas, B. Rivas-Murias, B. Rodríguez-González, M. Farle, V. Salgueiriño, *Nanoscale* 2018, **10**, 20462.
39 J. B. Yang, X. D. Zhou, W. B. Yelon, W. J. James, Q. Cai, K. V. Gopalakrishnan, S. K. Malik, X. C. Sun, D. E. Nikles, *J. Appl. Phys.* 2004, **95**, 7540.
40 P. Mendoza Zelis, G. A. Pasquevich, S. J. Stewart, M. B. Fernández van Raap, J. Aphesteguy, I. J.; Bruvera, C. Laborde, B. Pianciola, S. Jacobo, F. H. Sánchez. *J. Phys. D.: Appl. Phys.* 2013, **46**, 125006.
41 Z. Yang, J.-T. Jiang, C.-Y. Xu, Y. Wang, Y.-Y. Xu, L. Cao, L. Zhen, *Sci. Reports* 2017, **7**, 45480.
42 S. Ferrari, J. C. Aphesteguy, F. D. Saccone, *IEEE Trans Mag.* 2015, **51**, 2900206.
43 E. Wetterskog, C.-W. Tai, J. Grins, L. Bergström, G. Salazar-Álvarez, *ACS Nano* 2013, **7**, 7132.
44 J. B. Moussy, S. Gota, A. Bataille, M. J. Guittet, M. Gautier-Soyer, F. Delille, B. Dieny, F. Ott, T. D. Doan, P. Warin, P. Bayle-Guillemaud, C. Gatel, E. Snoeck, *Phys. Rev. B* 2004, **70**, 174448.
45 O. Margeat, M. Tran, M. Spasova, M. Farle, *Phys. Rev. B* 2007, **75**, 134410.
46 S. Morup, C. Frandsen, M. Fougt Hansen, *Beilstein J. of Nanotechnology* 2010, **1**, 48.
47 S. Blundell, *Magnetism in Condensed Matter*, Oxford University Press (New York) 2001.
48 W. Eerestein, T. T. M. Palstra, T. Hibma, S. Celotto. *Phys. Rev. B* 2002, **66**, 201101.
49 W. Eerestein, T. T. M. Palstra, T. Hibma, S. Celotto. *Phys. Rev. B* 2003, **68**, 014428.
50 F. Wang, V. N. Richards, S. P. Shields, W. E. Buhro, *Chem. Mater.* 2014, **26**, 5.
51 H. Zheng, R. K. Smith, Y.-w. Jun, C. Kisielowski, U. Dahmen, A. P. Alivisatos. *Science* 2009, **324**, 1309.

52 G. Kresse, J. Furthmüller, *Phys. Rev. B* 1996, **54**, 11169.
53 G. Kresse, J. Furthmüller, *Comput. Mater.Sci.* 1996, **6**, 15.

**Electronic Supplementary Information**

# Antiphase Boundaries in Truncated Octahedron-shaped Zn-doped Magnetite Nanocrystals

*Nerio Fontaiña-Troitiño,[1] Miguel A. Ramos-Docampo,[1] Martín Testa-Anta,[1]*

*Benito Rodríguez-González,[1] Manuel Bañobre-López,[2] Laura Bocher,[3]*

*Keith P. McKenna,[4] Verónica Salgueiriño[1]**

[1]Departamento de Física Aplicada and CACTI, Universidade de Vigo, 36310, Vigo (Spain)

[2]INL – Advanced (magnetic) Theranostic Nanostructures Lab, International Iberian Nanotechnology Laboratory, Av. Mestre José Veiga, Braga (Portugal)

[3]Laboratoire de Physique des Solides, Université Paris-Sud 91405 Orsay (France)

[4]Department of Physics, University of York, Heslington, York YO10 5DD (United Kingdom)

E-mail: vsalgue@uvigo.es

## Experimental Section

Zinc-doped magnetite ($Zn_xFe_{3-x}O_4$ ($x$ = 0.25 (sample ***1***), $x$ = 0.50 (sample ***2***), $x$ = 0.8 (sample ***3***), $x$ = 1.0 (sample ***4***))) nanoparticles were obtained by the simultaneous thermal decomposition of zinc and iron precursors (iron (II) acetate (Aldrich, 95%) and zinc (II) acetate dehydrated (Aldrich 98%)) in two different proportions (molar ratio; $Fe(ac)_2/Zn(ac)_2$ = 9.28 (sample ***1***), 5 (sample ***2***), 2.85 (sample ***3***) and 2 (sample ***4***)) to adjust the final stoichiometry. The process was carried out in all the cases using the hot-injection thermal decomposition, that is, injecting both precursors (dissolved in 5 mL of ethanol) in trioctyl amine (TOA) (25 mL, 57.18 mmol) at 180 °C and then left to reflux (at T = 300 °C) for two hours. Once cooled to room temperature, the nanoparticles were separated by centrifugation, washed several times with ethanol and finally dried at room temperature and stored.

Samples for (S)TEM were deposited on a carbon-coated copper grid. TEM images were obtained on a JEOL JEM 1010 microscope operating at 100 kV. (HR)TEM images were acquired on a JEOL JEM 2010F operating at 200 kV. The TEM images were used to obtain the size distribution considering few hundreds of nanoparticles in both samples. STEM-HAADF images were all acquired on the NION UltraSTEM200 operating at 100 kV, yielding a sub-ansgtröm probe size. The XRD patterns of the nanoparticles were obtained with a Phillips PANalytical X'Pert PRO diffractometer using a Cu-$K_\alpha$ radiation in a 2θ range from 20-100°. EDX spectroscopy and ICP analysis were used to determine the stoichiometry of the nanoparticles. Raman spectra were collected with a Renishaw in Via Reflex Raman Microscope. Experiments were conducted at room temperature by using two different excitation wavelengths, that is, $\lambda$ = 532 nm from a frequency doubled Nd:YAG and Nd:$YVO_4$ diode laser and $\lambda$ = 633 nm from a from a He-Ne laser. Magnetic measurements were performed using a Quantum Design (PPMS) magnetometer. Temperature-dependent magnetization curves of the samples were recorded from 5 to 300K at 5 mT under zero-field cooling (ZFC) and field-cooling (FC) conditions. Field-dependent magnetization curves were measured at $\mu_0 H$ = -5 to 5 T at 5 K and 300 K.

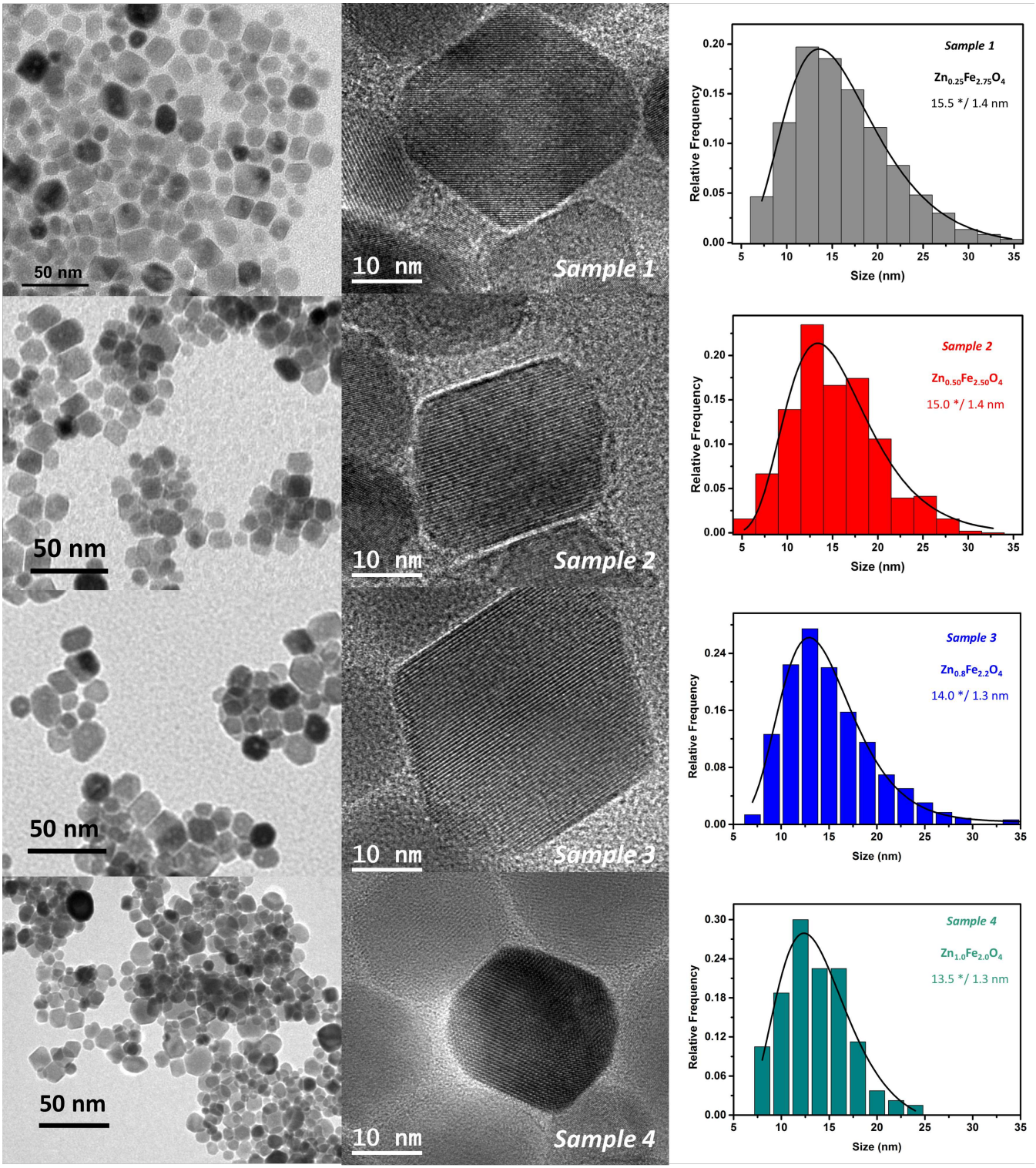


**Figure S1**. TEM (left column), HRTEM (central column) and size distribution (largest edge length) analysis fitted to lognormal functions (right column), of the zinc-doped magnetite nanocrystals from the four samples in consideration (from top to bottom, sample ***1*** to sample ***4***).

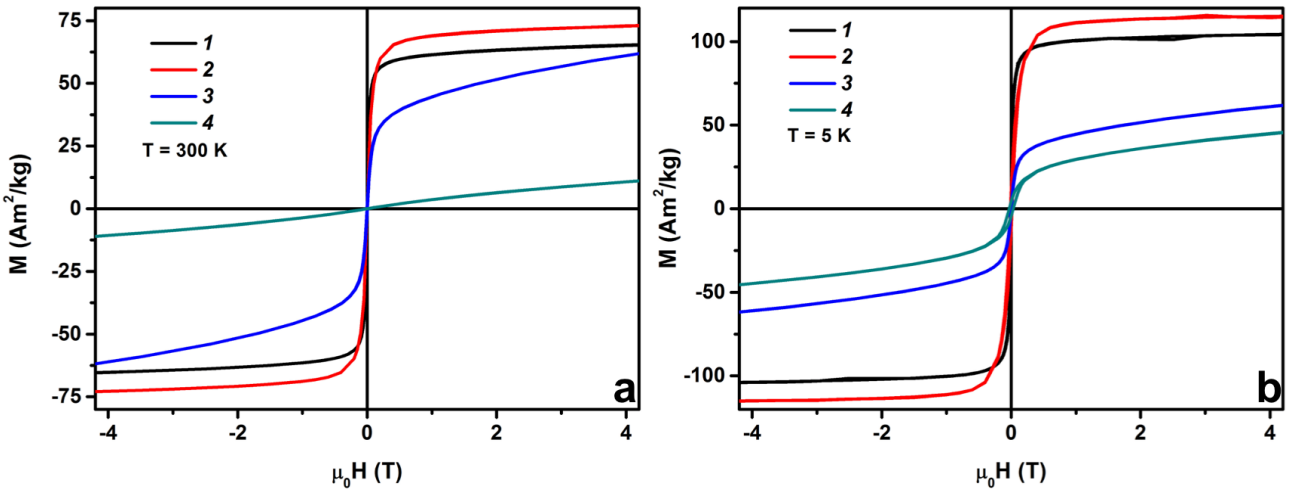


**Figure S2**. MvsH hysteresis loops at 300 K (a) and 5 K (b) of the zinc-doped magnetite nanocrystals from the four samples in consideration.

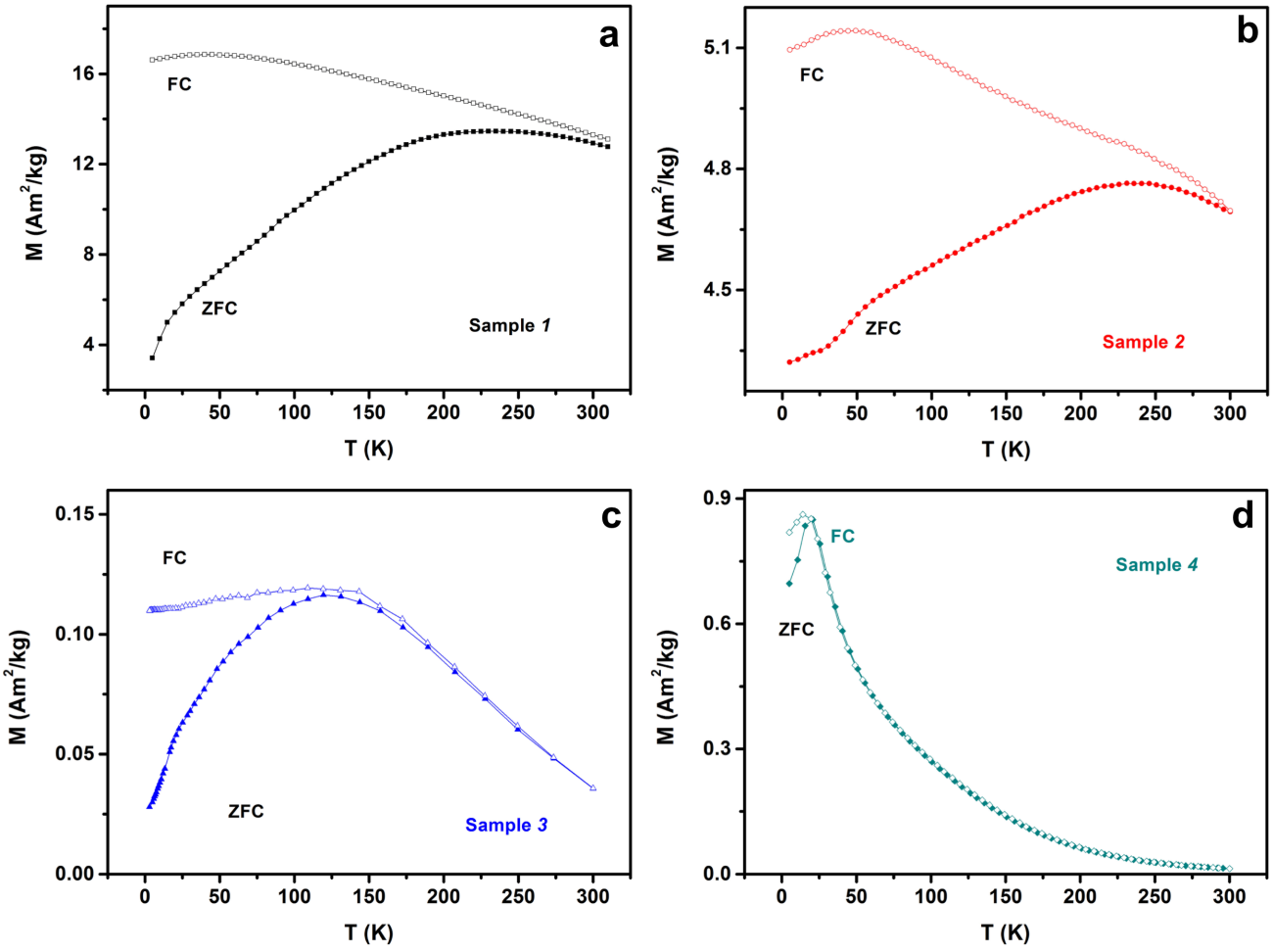


**Figure S3**. ZFC-FC Temperature-dependent magnetization of the zinc-doped magnetite nanocrystals from the four samples in consideration (sample ***1*** (a), sample ***2*** (b), sample ***3*** (c), and sample ***4*** (d)).

**Density functional theory (DFT) calculations**

Density functional theory (DFT) calculations to predict the structure, electronic and magnetic properties of bulk $Zn_xFe_{3-x}O_4$ using the projector augmented wave method as implemented in the Vienna *ab initio* simulation package were performed.[1,2] Predictions from several different levels of theory were compared including the Perdew, Burke, and Ernzerhof (PBE) approximation[3,] to exchange and correlation (both with and without Hubbard *U* corrections on Fe 3*d* states: *U*-*J*=3.8 eV – e.g. see reference 4) as well as the Heyd, Scuseria, and Ernzerhof (HSE) hybrid exchange-correlation functional.[5] The 3*s*, 3*d* electrons of Fe, and 2*s* and 2*p* electrons of O were treated as valence electrons and expanded in a plane wave basis with energies up to 400 eV. For primitive cell calculations on the end members $Fe_3O_4$ ($x$=0) and $ZnFe_2O_4$ ($x$=1) a gamma-centred 7x7x7 Monkhorst-Pack (MP) grid was used to sample to Brillouin zone. For the more demanding HSE calculations the MP grid was reduced to 6x6x6 with the Fock exchange potential sampled using a 2 x 2 x 2 grid. To model the compositions present in samples ***1*** and ***2*** ($Zn_2Fe_{22}O_{32}$ ($x$=0.25) and $Zn_4Fe_{20}O_{32}$ ($x$=0.50), respectively), a 2x2x1 supercell was employed and all symmetry inequivalent arrangements of Zn within the supercell were considered in order to identify the most stable. For all calculations a number of different orderings of the (collinear) Fe magnetic moments in order to identify the ground state magnetic structure were considered. The total energy was optimized with respect to the position of atoms and the unit cell dimensions using a conjugate gradients algorithm until all forces were less than 0.01 eV $Å^{-1}$. To predict the structure, stability and properties of the (111) antiphase boundary defects (APB) observed in the nanoparticles, a 336-atom supercell containing two domains each about 15 Å in extension perpendicular to the (111) plane was constructed. One domain was rigidly displaced by 3(*a*/4)(10-1) to create two antiphase boundary (APB) defects in the periodic supercell. The structure of the supercell was optimized with respect to the position of all atoms in the supercell using the methods described above but with a gamma-centred 2 x 2 x 2 MP grid. The total energy was also calculated for similar supercell

without the APB displacement (corresponding to a bulk crystal) in order to calculate the APB formation energy.

We first discuss the predicted properties of the two end members of the $Zn_xFe_{3-x}O_4$ series – $Fe_3O_4$ ($x$=0) and $ZnFe_2O_4$ ($x$=1) - at the different levels of theory. The Perdew, Burke, and Ernzerhof (PBE) approximation predicts $Fe_3O_4$ to be a half-metallic ferrimagnet with lattice constant a = 8.400 Å. The magnetic moment on the tetrahedral Fe (tet-Fe) sites is -3.48 $\mu_B$ while the moments on the octahedral Fe (oct-Fe) sites are 3.52 $\mu_B$ and 3.61 $\mu_B$. We note the electron density on the oct-Fe sites exhibits a slight disproportionation into two types of site hinting at an intrinsic instability towards a metal-insulator transition, i.e. the Verwey transition. PBE+$U$ also predicts $Fe_3O_4$ to be a half-metallic ferrimagnet with lattice constant a = 8.470 Å. The magnetic moment on the tet-Fe sites is -4.04 $\mu_B$ and between 3.67 and 4.25 $\mu_B$ on oct-Fe sites. The Heyd, Scuseria, and Ernzerhof (HSE) calculations performed using the PBE lattice constants predict very similar properties with magnetic moments on the tet-Fe sites of -4.07 $\mu_B$ and between 3.90 and 3.95 $\mu_B$ on the oct-Fe sites. PBE predicts the $ZnFe_2O_4$ to be an antiferromagnetic insulator with lattice constant a = 8.526 Å. The magnetic moments on the oct-Fe sites are ± 3.66 $\mu_B$ and ± 3.76 $\mu_B$ (again disproportioning into two types of site). The antiferromagnetic spin configuration is predicted to be 245 meV/formula unit more stable than the ferromagnetic state (i.e. $E_{FM}$-$E_{AF}$). PBE+$U$ predicts very similar results with a slightly larger lattice constant of a = 8.512 Å. The magnetic moments on the oct-Fe sites are ± 4.22 $\mu_B$ and ± 4.24 $\mu_B$. However, the antiferromagnetic spin configuration is predicted to be only 42 meV / formula unit more stable than the ferromagnetic state. Again, HSE calculations performed using the PBE lattice constants predict very similar properties with magnetic moments on the oct-Fe sites of ± 4.21 $\mu_B$ and ± 4.22 $\mu_B$. Overall the above results suggest that both PBE and PBE+$U$ give reasonable predictions for the stable magnetic configuration of $Zn_xFe_{3-x}O_4$ phases with the latter slightly more consistent with the predictions of HSE which is expected to be more accurate (especially for the insulating phases).

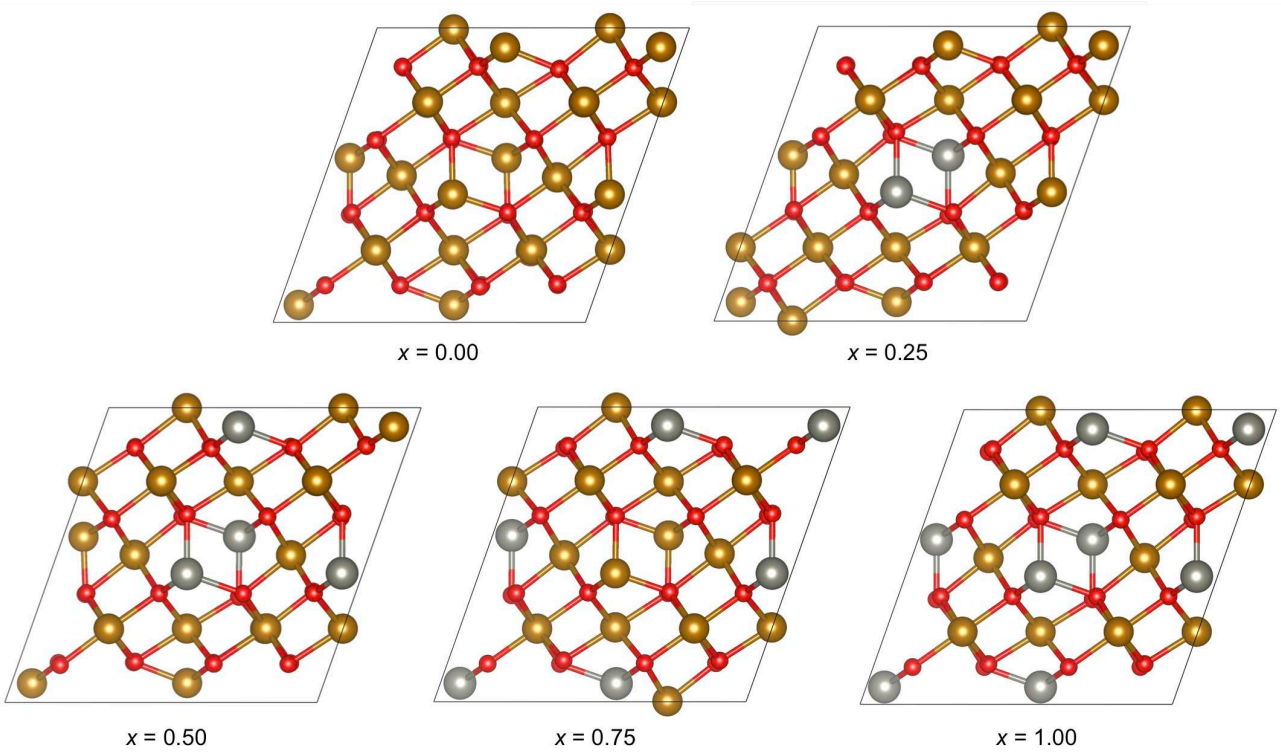


**Figure S2**. Optimized structures of $Zn_xFe_{3-x}O_4$ at the PBE+*U* level of theory using a 2x2x1 bulk supercell. Silver, brown and red spheres represent Zn, Fe and O atoms respectively.

**Table I:** Predicted properties of $Zn_xFe_{3-x}O_4$ at the PBE and PBE+*U* levels of theory.

| PBE | | | | |
|---|---|---|---|---|
| x | a (Å) | Magnetic order | Magnetization per formula unit (μB) | $E_{FM}$-$E_{AF}$ per formula unit (meV) |
| 0.00 | 8.400 | FM | 4.00 | 644 |
| **0.25** | 8.442 | FM | 5.49 | 389 |
| **0.50** | 8.484 | FM | 6.87 | 178 |
| 0.75 | 8.484 | FM | 8.11 | 275 |
| 1.00 | 8.526 | AF | 0.00 | -245 |
| **PBE + U** | | | | |
| x | a (Å) | Magnetic order | Magnetization per formula unit (μB) | $E_{FM}$-$E_{AF}$ per formula unit (meV) |
| 0.00 | 8.470 | FM | 4.00 | >244 |
| **0.25** | 8.512 | FM | 5.50 | 249 |
| **0.50** | 8.512 | FM | 7.00 | 121 |
| 0.75 | 8.555 | FM | 8.50 | 22 |
| 1.00 | 8.512 | AF | 0.00 | -42 |

The optimized structures (including optimization of cell volume to within 0.5%) and energies for all symmetry inequivalent arrangements of Zn in a 2x2x1 expansion of the primitive bulk supercell are obtained at both the PBE and PBE+*U* levels of theory. The results are broadly consistent between both levels of theory and figure S2 shows the most stable structures obtained using PBE+*U*. For all compositions there is a preference for Zn to distribute homogeneously throughout the bulk with no evidence of clustering. Zn substitutes for tetrahedral Fe sites and there is a small expansion of the lattice constant associated with increasing Zn content (see Table I). For $x < 1.00$ all structures are predicted to be ferrimagnetic with antiparallel alignment of the moments on the tetrahedral and octahedral Fe sublattices (with the latter being more numerous). As the Zn content increases there is a progressive increase in the total magnetic moment as a result of the reduction in net moment associated with the tetrahedral sites. However, for $x = 1.00$ the antiferromagnetic configuration becomes more stable. We have calculated the energy difference between the ferrimagnetic and antiferromagnetic spin configurations as a function of $x$ at both the PBE and PBE+*U* levels of theory (see $E_{FM}$-$E_{AF}$ in Table I). A clear crossover between ferrimagnetic and antiferromagnetic order between $x$=0.75 and $x$=1.00 is predicted.

**References**


1. Kresse G.; Furthmüller, J. *Phys*. *Rev*. *B* **1996**, *54*, 11169.

2. Kresse G.; Furthmüller, J. *Comput*. *Mater*.*Sci*. **1996**, *6*, 15-50.

3. Perdew, J. P.; Burke, K.; Ernzerhof, M. *Phys*. *Rev*. *Lett*. **1996**, *77*, 3865-3868.

4. McKenna, K. P.; Hofer, F.; Gilks, D.; Lazarov, V. K.; Chen, C.; Wang Z.; Ikuhara, Y. *Nature Comm*. **2014**, *5*, 5740.

5. Heyd, J.; Scuseria, G. E.; Ernzerhof, M. *J*. *Chem*. *Phys*. **2003**, *118*, 8207-8215.